



Empirical-Statistical Modeling and Prediction of Geometric Characteristics for Laser-Aided Direct Metal Deposition of Inconel 718 Superalloy

Saeedeh Jelvani¹ · Reza Shoja Razavi² · Masoud Barekat¹ · Mohammadreza Dehnavi¹

Received: 10 March 2019 / Accepted: 3 July 2019 / Published online: 23 July 2019
© The Korean Institute of Metals and Materials 2019

Abstract

It is requisite in laser-aided direct metal deposition (LADMD) to investigate the influence of three key process parameters (laser power, scanning speed, and powder feeding rate) on geometric characteristics of single-track deposits so as to acquire LADMD deposits with minimum defects and controlled geometric accuracy. In this study, LADMD of Inconel 718 superalloy was studied and the dependency of geometric characteristics on key process parameters was investigated as a combined parameter ($P^\alpha V^\beta F^\gamma$). A simple empirical-statistical modeling was used employing linear regression method. The results showed that the geometric characteristics had a linear relationship with a combined parameter including three/two key process parameters together. The height and wetting angle of single-track deposits were dependent on $P^2 V^{-1} F^1$ and $P^{3/2} V^{-1} F^1$, respectively. The width of single-track deposits was dependent on $P^2 V^{-1/4}$ but it was independent of powder feeding rate. The dilution of single-track deposits depended on $V^1 F^{-1}$ while laser power had no effect on it. A process map is developed to enable optimization of the process parameters in LADMD process of Inconel 718.

Keywords Additive manufacturing (AM) · Laser-aided direct metal deposition (LADMD) · Inconel 718 · Geometric characteristics · Linear regression

1 Introduction

Inconel 718 is a nickel-based superalloy that is widely used in gas turbines and jet engines at working temperatures above 650 °C. The high-temperature strength of this alloy is predominantly due to the precipitation of γ'' phase (Ni_3Nb) with a BCT structure in continuous γ phase matrix with an FCC structure. Furthermore, gamma- γ' phase ($\text{Ni}_3(\text{Al}, \text{Ti})$) with an FCC structure causes greater strength for the alloy [1–4].

Additive manufacturing (AM) is one of the 3D printing methods that is capable of building a component from a computer-aided design (CAD) [5, 6]. In recent years, many research studies have focused on AM field, in particular,

direct metal deposition (DMD) [7, 8]. At present, the development of AM focuses on the production of metal components, alloys and complex metal matrix composites that meet the requirements of aerospace, defense, automotive, and medical industries. The layer-by-layer manufacturing technology for meltable powders was reported by Ciraud [9], which is considered as a pioneer in this field. Laser-aided direct metal deposition (LADMD) is one of AM methods in which the injection of metal powder simultaneously happens with the irradiation of laser beam and layer-by-layer metal deposition is applied. LADMD is a suitable method that can be used to build up hot-section components of gas turbines.

The complexity of manufacturing and the high cost of manufacturing of new parts bring about the need for repair of damaged components. One of the most advanced and reliable technique to repair damaged parts is LADMD. When it comes to the build-up and repair of IN718 superalloy, the most important feature is the absence of structural defects and the achievement of a uniform structure. Due to the fact that the geometrical characteristics of the deposits have an important effect on the final properties and possible formation of defects, investigating the geometric characteristics

✉ Masoud Barekat
m.barekat@mut-es.ac.ir

¹ Department of Materials Engineering, Malek Ashtar University of Technology, Shahin Shahr, Isfahan, Iran

² Faculty of Materials and Manufacturing Engineering, Malek Ashtar University of Technology, Tehran, Iran

of single-track deposits (height, width, dilution, and wetting angle) is an appropriate measure for determining the quality of deposits.

In LADMD, three parameters of laser power (P) [w], scanning speed (V) [mm/s], and powder feeding rate (F) [mg/s] have the greatest effect on the quality of deposits and are key process parameters. However, other process parameters such as laser beam energy distribution, amount and type of shielding gas and powder carrier gas, powder size, and angle of powder injection are effective on the quality of deposits. It is also important to obtain the interconnection among key process parameters (P , V , and F) and relate the interconnections to the geometric shape of deposits so as to optimize the process. For this purpose, empirical-statistical models have been considered since 2003 [10–23]. In recent years, Barekat et al. [19] investigated laser cladding of Co–Cr–Mo alloy on a γ -TiAl substrate and presented an empirical-statistical model. In another study, Ansari et al. [20] presented an empirical-statistical model for laser cladding of NiCrAlY powder on Inconel 718 superalloy. Moreover, Ansari et al. [20] summarized all empirical-statistical reports in the form of a table and concluded that empirical-statistical models differ for various powder/substrate combinations.

Given previous research studies, the empirical-statistical modeling for LADMD of Inconel 718 has not been performed yet. On the other hand, none of the research studies examined the effect of key process parameters on the geometric characteristics. The present study aims to investigate the interconnection of key process parameters (P , V , and F) and predict geometric characteristics of deposits using an empirical-statistical model. The process map designed by this model can be a useful guide for reducing the range of process parameters and the number of experiments needed to achieve optimal process parameters.

2 Materials and Methods

Inconel 718 commercial powder (Sulzer Metco USA) was used. The powder has a spherical morphology with a grain size of $45 \pm 15 \mu\text{m}$. Figure 1 shows the morphology of Inconel 718 powder. Inconel 718 cast superalloy is used as the substrate. Circular plates of the substrate with a diameter of 15 mm and a thickness of 5 mm were prepared and then cleaned with acetone. Figure 2 shows the microstructure of Inconel 718 substrate. The chemical composition of Inconel 718 alloy for both the substrate and powder obtained with optical emission spectroscopy (OES) is presented in Table 1.

The LDMD process was performed using a pulsed Nd:YAG laser (IQL20 model with 700 W maximum power). The use of pulsed Nd:YAG laser has been reported to be beneficial for material processing and manufacturing

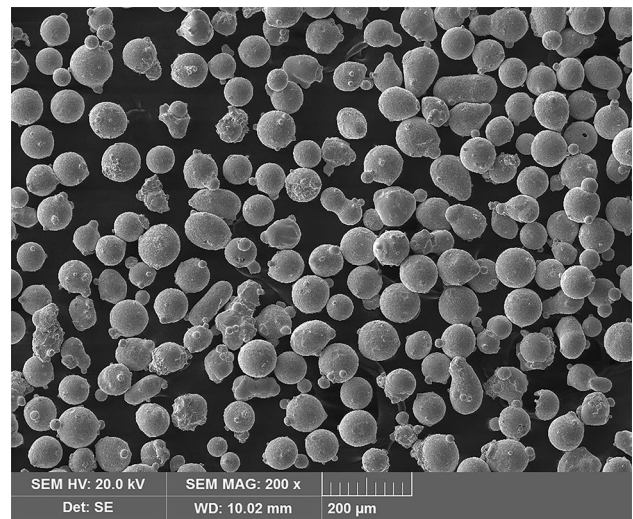


Fig. 1 SEM images showing the morphology of Inconel 718 powder

[24]. The output pulses of this laser have a standard square shape. Accessible parameters in this laser are frequency of 1–250 Hz, pulse width 0.25–25 ms, and pulse energy 0–70 J. During LDMD, a power meter of A-500 W-Lp Ophir model was used to measure the average power. The diameter of the laser beam (1 mm) was set according to the laser nozzle distance, which was constant for all samples. The laser beam energy distribution in all samples is Gaussian (TEM₀₀). According to the design of powder injection nozzle, the angle of powder injection with the laser beam is 30°. Argon gas was used as shielding and powder carrier gas at a pressure of 20 and 15 L per minute, respectively. According to the previous research studies and preliminary screening tests, average laser power (P) was set at four levels, scanning speed (V) was set at three levels, and powder feeding rate (F) was set at five levels. Effective parameters and selected levels are listed in Table 2. The single-track LDMD process was conducted using 60 different groups of parameters in the form of a full-factorial experiment. Table 3 shows these 60 groups of different parameters. The samples were named INC (i), which refers to single-track deposits of Inconel 718 generated by an i -th group of parameters.

In order to evaluate the geometric characteristics, the transverse cross-section of single-track deposits was investigated. The single-track deposits were cut, ground and then polished with 1- μm alumina powder. In order to etch the samples, an electro-etching process was used with a voltage of 10 V, and a solution of 1 g chromic acid (CrO₃) and 10 ml distilled water for 8 s at ambient temperature. To study the morphology of initial powder and the cross-sections of deposits, a scanning electron microscope (SEM) (MIRA3, TESCAN) was used. Figure 3 shows the geometric shape of a single-track deposit in the form of a schema. The height (h), width (w), wetting angle (θ) and depth of penetration

Fig. 2 SEM images showing microstructure of Inconel 718 substrate

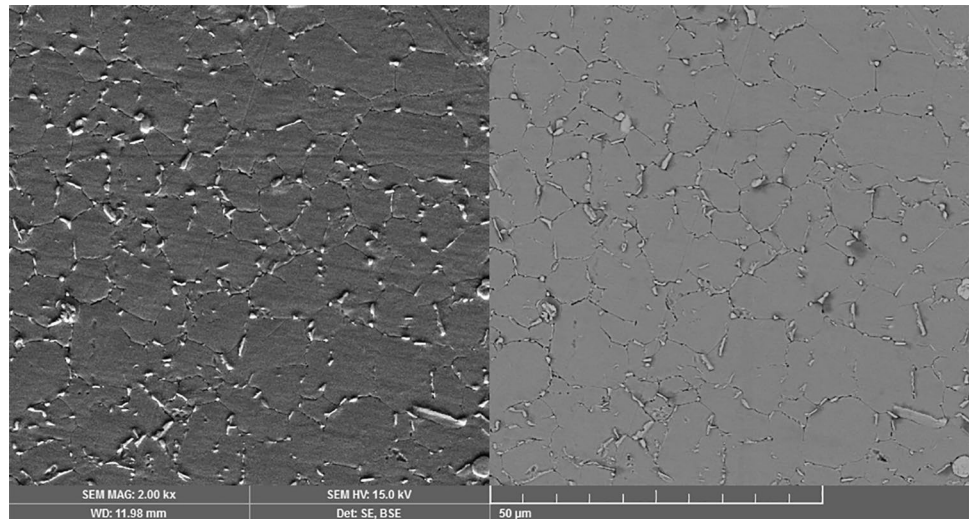


Table 1 Chemical composition of Inconel 718 alloy used as substrate and powder

Material	Form	Element (wt%)									
		Ni	Fe	Cr	Nb	Co	Al	Ti	Mo	Ta	C
Inconel 718	Powder	Bal.	21	14.7	6.82	0.42	0.65	0.78	2.56	–	0.05
Inconel 718	Plate	Bal.	17.25	19	6.88	0.8	0.6	1.1	3	0.05	0.05

Table 2 Effective parameters and selected levels for LADMD

Parameters	Levels
P (W)	150, 200, 250, 300
V (mm/s)	4, 5, 6
F (mg/s)	150, 200, 250, 300, 400

of the deposit in the substrate (b) were measured according to SEM images for all 60 samples. The measurements are presented in Table 3. The geometric method [Eq. (1)] was used to determine the dilution (D) [25].

$$D(\%) = \frac{b}{h + b} \quad (1)$$

For empirical-statistical modeling, geometric characteristics including h , w , D , b , and θ were considered separately as dependent variables (y). The combined parameter $P^\alpha V^\beta F^\gamma$ was assumed as an independent variable (x). The linear regression equation was calculated from Eq. (2).

$$y = a(P^\alpha V^\beta F^\gamma) + b \quad (2)$$

In this equation, a and b are constants, powers α , β , and γ were determined by using trial and error method with the best linear correlation coefficient between dependent and independent variables. The line equation for each geometric characteristic was extracted in terms of a combined parameter. Finally, a process map was plotted based on the

combined parameters. For plotting this map, the geometric characteristics [y in Eq. (2)] were considered as constant values (shown in the plot) and the values of P in different ratios of F/V were calculated according to the corresponding line equation. The trend-line of P values formed the curves in the plot.

After identification of the optimal region in the processing window, six different single-wall deposits were produced using six sets of process parameters within the optimal region. The Z-increment between layers was 0.2–0.4 mm for single-wall samples.

3 Results and Discussion

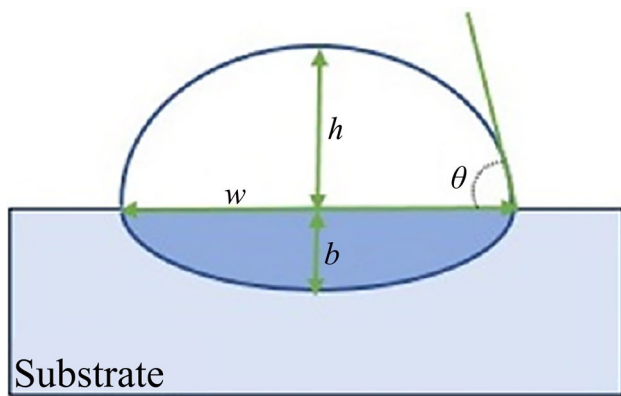
Figure 4 shows SEM images of the transverse cross-section of single-track deposits at laser powers of 150, 200, 250, and 300 W, respectively. In this figure, scanning speed increased from left to right, and powder feeding rate increased from up to down. Investigation and comparison of the geometric characteristics of single-track deposits can show some qualitative features. By increasing scanning speed, the height, width, and wetting angle reduced; however, the dilution increased. By increasing powder feeding rate, the height increased but the dilution, penetration depth, and wetting angle decreased. Increasing laser power could increase the height, width, penetration depth, and wetting angle while the dilution was not much affected. According to Fig. 5,

Table 3 60 groups of different parameters for LADMD and geometric characteristics in each group

Track	Processing parameters			Geometric measurements					Porosity percentage
	<i>P</i> (W)	<i>V</i> (mm/s)	<i>F</i> (mg/s)	<i>h</i> (mm)	<i>w</i> (mm)	θ (°)	<i>b</i> (mm)	<i>D</i> (%)	
INC (1)	150	4	150	0.126	1.26	9.5	0.221	64	1
INC (2)	150	5	150	0.096	1.202	8	0.251	72	0.34
INC (3)	150	6	150	0.045	1.256	6	0.228	84	0.00
INC (4)	150	4	200	0.163	1.285	20.25	0.172	51	0.64
INC (5)	150	5	200	0.110	1.260	17.8	0.198	64	0.00
INC (6)	150	6	200	0.098	1.234	16.3	0.200	67	0.00
INC (7)	150	4	250	0.222	1.250	19.34	0.148	40	0.29
INC (8)	150	5	250	0.137	1.276	12.85	0.161	54	0.29
INC (9)	150	6	250	0.129	1.222	11.43	0.161	56	1.23
INC (10)	150	4	300	0.220	1.249	23.5	0.150	41	1.60
INC (11)	150	5	300	0.160	1.244	12.3	0.128	44	0.00
INC (12)	150	6	300	0.130	1.189	17	0.132	50	0.00
INC (13)	150	4	400	0.245	1.300	25.5	0.108	31	4.10
INC (14)	150	5	400	0.195	1.239	23.5	0.104	35	0.00
INC (15)	150	6	400	0.158	1.225	17.5	0.116	42	0.00
INC (16)	200	4	150	0.216	1.428	18	0.296	58	1.60
INC (17)	200	5	150	0.113	1.428	19	0.274	71	0.90
INC (18)	200	6	150	0.090	1.396	18	0.297	77	3.40
INC (19)	200	4	200	0.184	1.341	19.8	0.199	52	0.00
INC (20)	200	5	200	0.132	1.392	16	0.208	61	0.00
INC (21)	200	6	200	0.104	1.344	11	0.224	68	0.65
INC (22)	200	4	250	0.270	1.440	20	0.258	49	0.60
INC (23)	200	5	250	0.226	1.408	17	0.248	52	4.60
INC (24)	200	6	250	0.133	1.404	13.7	0.206	61	0.01
INC (25)	200	4	300	0.324	1.372	31.3	0.232	42	1.40
INC (26)	200	5	300	0.304	1.441	33	0.222	42	2.30
INC (27)	200	6	300	0.244	1.393	26	0.204	46	0.00
INC (28)	200	4	400	0.548	1.389	50	0.192	26	1.10
INC (29)	200	5	400	0.428	1.342	38	0.197	32	1.50
INC (30)	200	6	400	0.254	1.381	36.7	0.170	40	0.22
INC (31)	250	4	150	0.274	1.572	24	0.395	59	2.60
INC (32)	250	5	150	0.218	1.497	25	0.420	66	1.70
INC (33)	250	6	150	0.107	1.508	21.6	0.436	80	2.50
INC (34)	250	4	200	0.409	1.525	40.7	0.321	44	1.40
INC (35)	250	5	200	0.305	1.552	34.6	0.360	54	1.30
INC (36)	250	6	200	0.211	1.543	34	0.340	62	2.30
INC (37)	250	4	250	0.324	1.500	40	0.282	47	1.80
INC (38)	250	5	250	0.332	1.564	29.6	0.296	47	3.90
INC (39)	250	6	250	0.204	1.536	19	0.312	60	1.00
INC (40)	250	4	300	0.540	1.539	50	0.282	34	4.10
INC (41)	250	5	300	0.408	1.477	40	0.292	42	2.70
INC (42)	250	6	300	0.254	1.489	29	0.263	51	1.60
INC (43)	250	4	400	0.802	1.548	65	0.270	25	2.40
INC (44)	250	5	400	0.657	1.537	52	0.272	29	1.20
INC (45)	250	6	400	0.456	1.530	42	0.251	36	0.90
INC (46)	300	4	150	0.230	1.710	25.98	0.480	68	0.00
INC (47)	300	5	150	0.132	1.650	18.37	0.503	79	0.00
INC (48)	300	6	150	0.100	1.700	14.63	0.516	84	0.00
INC (49)	300	4	200	0.523	1.690	54	0.470	47	1.00

Table 3 (continued)

Track	Processing parameters			Geometric measurements					Porosity percentage
	P (W)	V (mm/s)	F (mg/s)	h (mm)	w (mm)	θ (°)	b (mm)	D (%)	
INC (50)	300	5	200	0.373	1.596	42	0.468	56	1.40
INC (51)	300	6	200	0.284	1.601	28.6	0.462	62	0.00
INC (52)	300	4	250	0.668	1.730	53.12	0.426	39	1.00
INC (53)	300	5	250	0.483	1.700	51.24	0.402	45	0.85
INC (54)	300	6	250	0.284	1.670	37	0.386	58	0.00
INC (55)	300	4	300	0.602	1.648	63	0.35	37	0.10
INC (56)	300	5	300	0.531	1.617	55	0.341	39	1.90
INC (57)	300	6	300	0.468	1.635	46.6	0.333	42	1.80
INC (58)	300	4	400	0.909	1.632	82.7	0.341	27	0.50
INC (59)	300	5	400	0.79	1.583	73	0.306	28	1.20
INC (60)	300	6	400	0.596	1.595	62	0.322	35	1.50

**Fig. 3** Schematic illustration of single-track deposit; h is height, w is width, b is depth of penetration, and θ is wetting angle

by increasing powder feeding rate and decreasing scanning speed, the height increased. Similarly, laser power had a significant effect on it. The effect of laser power can be justified in such a way that the temperature increases with increasing laser power, resulting in more powder melting and increasing the height of single-track deposits. Also, the distribution of powder particle size and the phenomenon of laser beam attenuation can affect the absorbed energy level during LADMD and change the height of deposits [26–28]. The effect of powder feeding rate and scanning speed is that the amount of powder injected per unit area increases with increasing powder feeding rate and decreasing scanning speed (increasing F/V ratio). As a result, more amount of powder melts and the height of deposit increases.

Using regression method, the linear relationship between h and key process parameters of P , F and V was obtained. In Fig. 6a, the relationship is plotted. The distribution of residuals in relation to the normal line is plotted in Fig. 6b. The regression coefficient of $R=0.96$ shows that linear

relationship exists. The resulting regression line equation was obtained as follows.

$$h = 1.94E - 06(P^{3/2}V^{-1}F^1) - 5.30E - 02$$

A minimum height of 90 μm was achieved at highest scanning speed and lowest laser power, and a maximum of 900 μm was achieved at lowest scanning speed and highest laser power. Therefore, the height is mainly controlled by a combined parameter obtained from P , F , and V . Although various substrate/powder combinations have different combined parameters, the proposed model in this study is consistent with the majority of previous research studies on empirical-statistical models [10, 12, 14–17, 22, 23]. However, some studies have reported the height as a function of F and V [11, 13, 19].

In Fig. 7, the width of single-track deposits (w) is plotted in accordance with the changes in three key parameters. As can be seen, the width increases with increasing laser power. This increase is linear. As scanning speed decreases, the width decreases. As can be seen, powder feeding rate had an insignificant effect on the change in width. The width of deposits at same values of laser power and scanning speed but different values of powder feeding rate is approximately equal. The effect of powder feeding rate in width can be seen by overlapping of the data points. When the data points overlap, it shows the effect of powder feeding rate is negligible. These results can be attributed to the presence of external and internal forces in the melt pool. In laser-aided processes, external and internal forces interfere in the formation of melt pool. External forces mainly depend on the design of the nozzle, the powder flow, and the pressure of the carrier and shielding gas. The internal forces are usually a combination of two buoyancy and Marangoni forces. Buoyancy force is due to the difference in the density of the liquid in melt pool and Marangoni force forms in the absence of a surface active agent that is dependent on the surface tension gradient in the melt pool. In LADMD process, laser as a source of heat

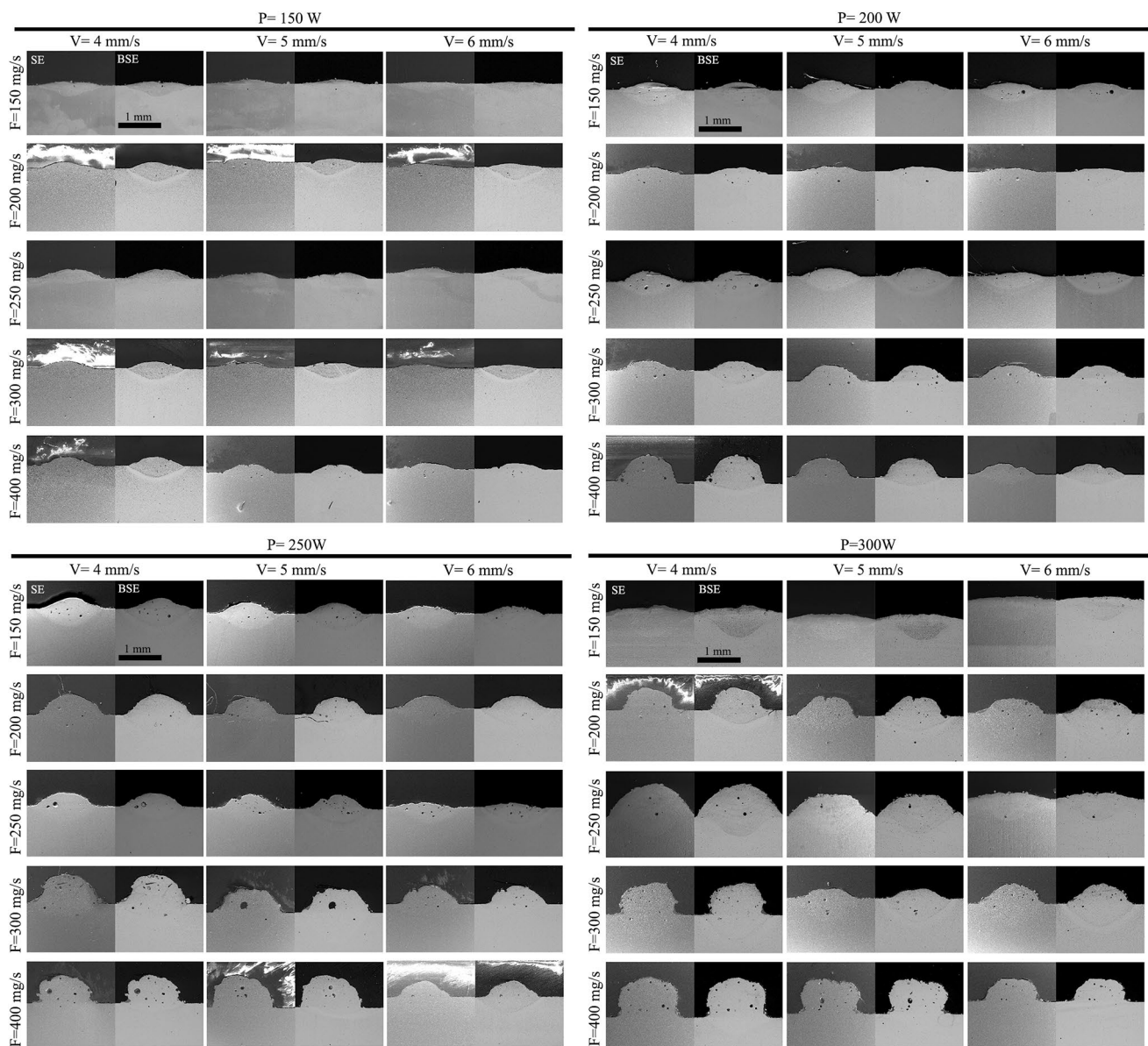


Fig. 4 SEM images of cross section of single-track deposits with different laser power, scanning speed and powder feeding rate

causes the center of the melt pool to become warmer than the edge areas. Since the warmer metal in the center has less surface tension, the liquid metal moves from the center towards the cooler sides with less surface tension. This surface tension gradient at the surface of the melt pool can cause a shear stress from the center to the edges. In the area below the surface, the melted metal flows in the opposite direction from the edges towards the center. With increasing laser power, the heat in the center of the melt pool is more than the edges, and by creating a surface tension gradient, the melted metal moves at the surface towards the edges. As a result, the width of the melt pool increases with increasing laser power. As scanning speed decreases, the reaction time

between the laser beam and the material increases. As a result, the input energy increases and according to the above-mentioned explanations, creating a surface tension gradient between the center and the edges, thereby extending the melt pool towards the edges and increasing the width of the melt pool. Using linear regression method, the relationship between w and key parameters of P , F and V was obtained. In Fig. 8a, this relationship is plotted. Distribution of the residuals compared to the normal line is plotted in Fig. 8b. The high regression coefficient ($R=0.97$) shows the accuracy of the line equation and the combined parameter. The linear equation between w and the combined parameter was obtained as follows.

Fig. 5 The height as a function of key process parameters

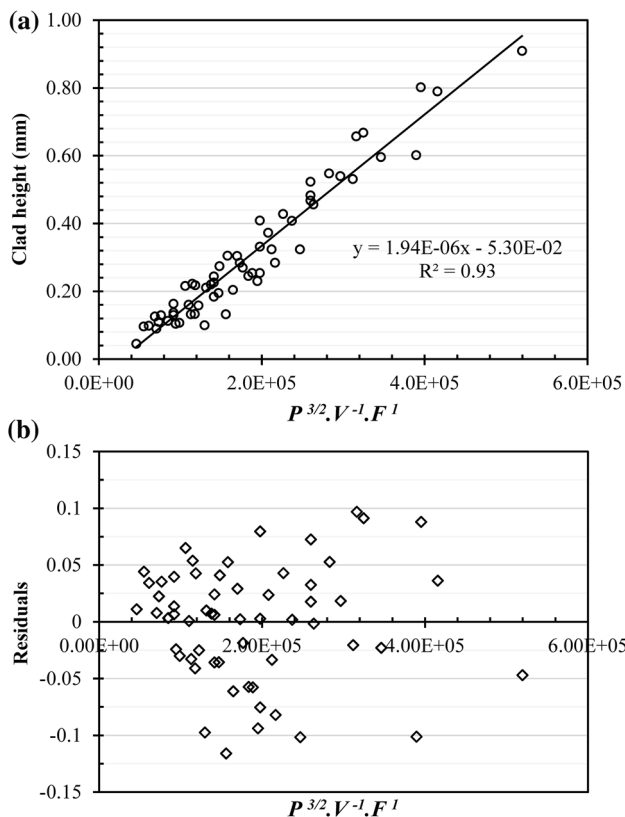
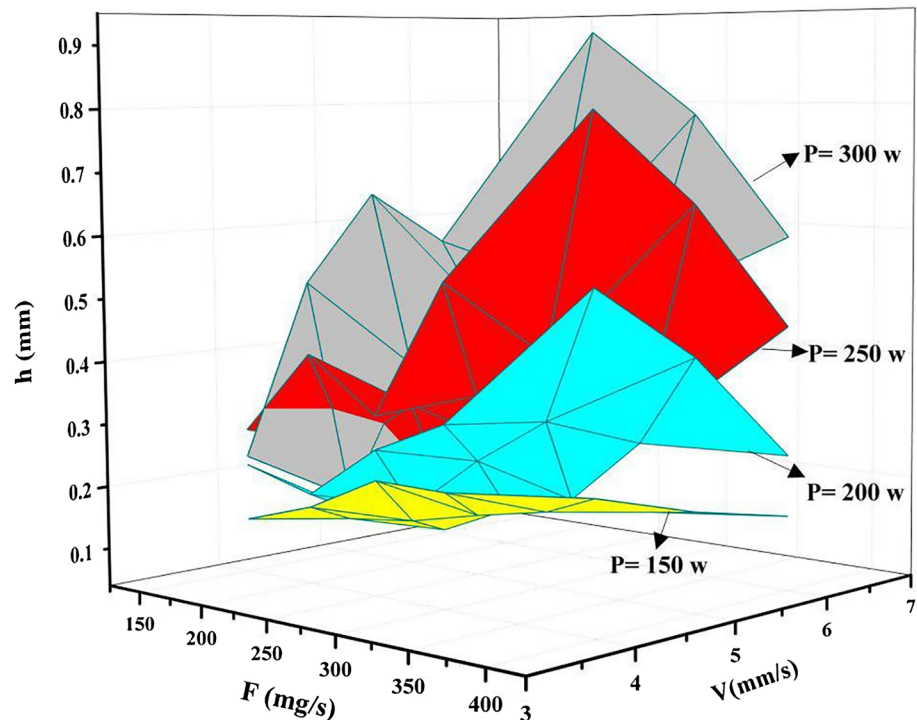


Fig. 6 **a** Dependency of the height on the combined parameter $P^{3/2}V^{-1}F^1$, and **b** residual plot

$$w = 8.77E - 06(P^2V^{-1/4}) + 1.14E + 00$$

The comparison of this study with previous research studies shows that laser power and scanning speed are most effective on the width while the effect of powder feeding rate is negligible [11, 13, 16, 18, 19, 22, 23].

The depth of penetration and dilution are two important characteristics in LADMD. The reason for the importance of these two characteristics is that the amount of melting material in the underlying deposit is important in the process. Adequate penetration of the upper deposit in the underlying deposit and proper dilution are important aspects. The presence of dilution creates a metallurgical bond between the deposits and ensures their adhesion to each other. The penetration bond between the deposits occurs by fusion. The fusion bond is usually strong and has a high resistance to mechanical and thermal shocks, provided that there is no combination of high tension at the interface. Therefore, there is a need for fusion, but the high values are unnecessary. Change in the depth of penetration (*b*) is plotted as a function of three key process parameters in Fig. 9. It is observed that the depth of penetration increases with increasing laser power and decreasing powder feeding rate. The reason for this is to increase the input energy by increasing laser power, resulting in an increased absorbed energy by the substrate and a greater amount of substrate melts. On the other hand, as already mentioned, one of the most influential forces in the process is buoyancy force. With increasing laser power,

Fig. 7 The width as a function of key process parameters

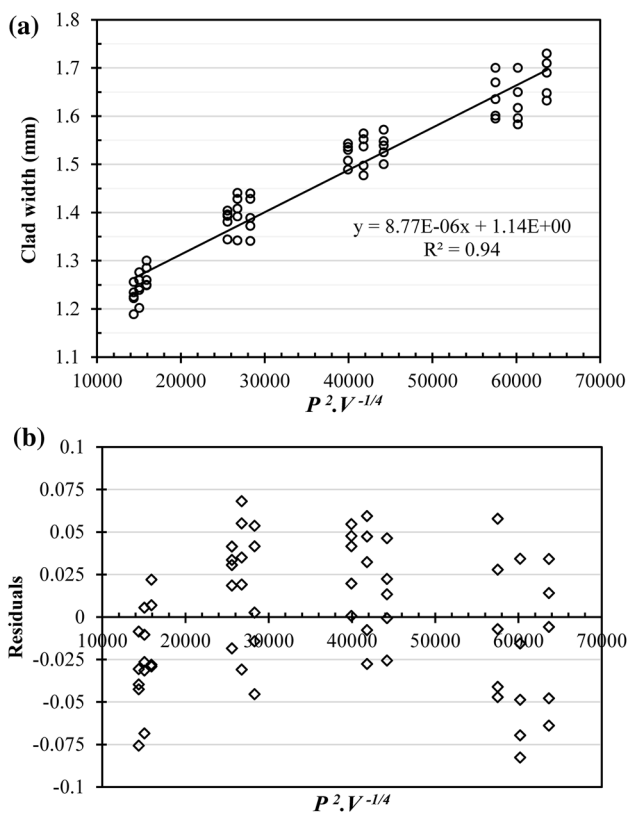
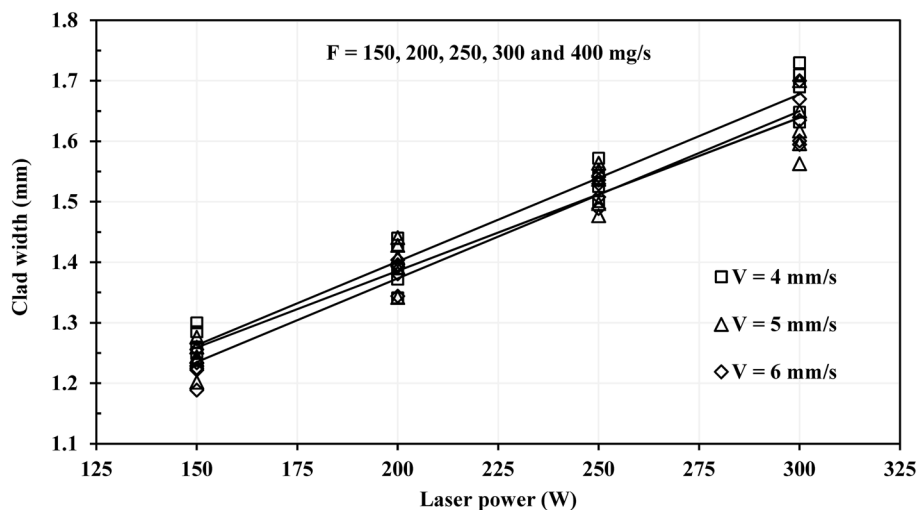


Fig. 8 **a** Dependency of the width on the combined parameter $P^2V^{-1/4}$, and **b** residual plot

the liquid metal in the center of the melt pool is warmer than the interface of the melt pool. Given that density is a function of material’s temperature, density decreases with increasing temperature. The gravity force causes the heavier liquid metal to move down (melt-solid interfaces) and create a melt convection. This convection causes the heat and mass transfer in the melt pool. Grashof number

(Gr) expresses the ratio of buoyancy force to viscous force. Given the fact that Gr is directly related to ΔT , as laser power increases, ΔT increases and Gr increases. The larger Gr number indicates that buoyancy force is dominant. On the other hand, Gr number has a direct relation to the liquid metal density. With increasing laser power, the depth of penetration increases. The ratio of Marangoni number to Grashof number provides a dimensionless number ($R_{S/B}$). The higher Grashof number and/or lower $R_{S/B}$ number, the deeper melt pool [29].

Figure 10a shows the relationship between b and the combined parameter P^2F^{-1} . Figure 10b shows the distribution of the residuals to the normal line for this relationship. The obtained regression coefficient for the proposed linear model is $R=0.96$, which shows high accuracy of the model. The linear equation was obtained between b and the combined parameter is written as follows.

$$b = 7.36E - 04(P^2F^{-1}) + 1.10E - 01$$

Comparing the results of the present model with those of previous research studies indicates that the present model is in line with some of the previous research studies on the empirical-statistical model [12, 16].

According to Fig. 11, the dilution increases with increasing scanning speed and decreasing powder feeding rate, while increasing or decreasing the laser power has no effect on the dilution. If laser power had a significant impact on the dilution, the dilution values for deposits with different laser power levels and the same values of powder feeding rate and scanning speed would not have been approximately equal to each other (they would not have been overlapped). However, the single-track deposits have a more or less equal dilution values in the same amounts of powder feeding rate and scanning speed. Therefore, only the combined parameter obtained from F and V can largely control the dilution. The dilution of 25%, observed at highest powder feeding rate and

Fig. 9 The depth of penetration as a function of key process parameters

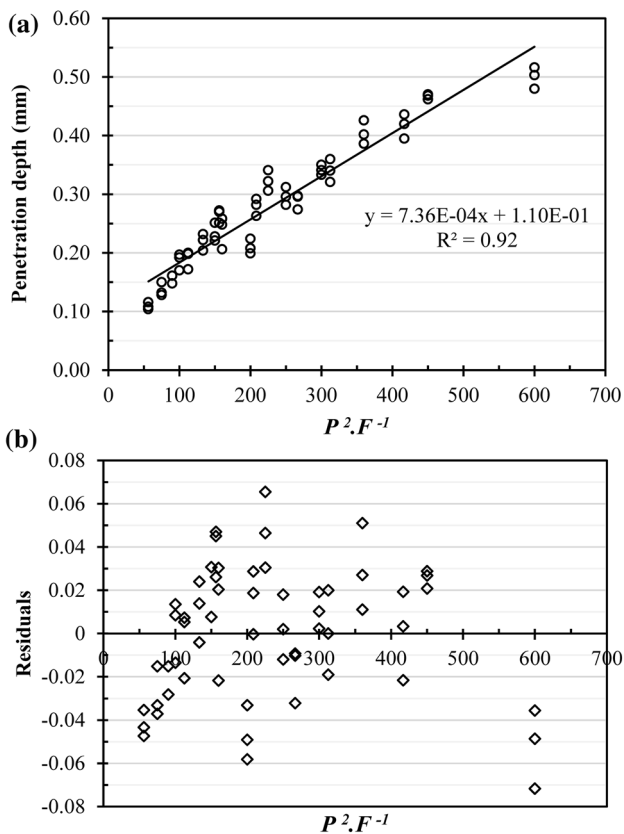
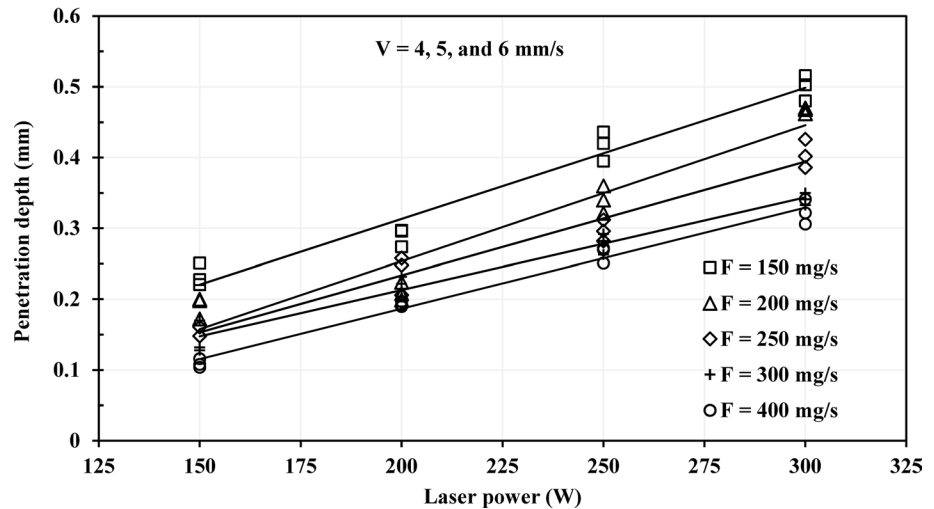


Fig. 10 **a** Dependency of the depth of penetration on the combined parameter P^2F^{-1} , and **b** residual plot

lowest scanning speed, varied to 85%, observed at highest scanning speed, and lowest powder feeding rate.

Using linear regression method, the relationship between the dilution (D) and key parameters of F and V was obtained. In Fig. 12a, the relationship is plotted with a linear regression coefficient of $R = 0.96$. The plot for the distribution of

the residuals relative to the normal line in accordance with the combined parameter of V^1F^{-1} is shown in Fig. 12b. The line equation according to regression analysis is as follows.

$$D = 1.80E + 03(V^1F^{-1}) + 1.23E + 01$$

As mentioned in Eq. (1), the dilution is the result of dividing the height into the sum of the height and depth of penetration. Since both factors determining the dilution (i.e. height and depth of penetration) depend on laser power parameter, the effect of laser power parameter can be eliminated by simplifying the numerator and the denominator of the fraction in the dilution formula. Comparing the relationships obtained in this study with those of previous research studies indicates that some other researchers also came up with a combined parameter including V and F [15, 20, 23].

According to Eq. (1), the dilution depends on the depth of penetration and height; therefore, these two factors should be simultaneously considered in order to explain the statistical relationship for dilution. By reducing scanning speed, the reaction time between the laser beam and the material increases and the input energy to the substrate increases, which increases the depth of penetration. In contrast, reducing scanning speed increases the height. As a result, the dilution increases. The effect of powder feeding rate on the depth of penetration and dilution is significant so that the amount of powder reached the substrate per unit time increases with increasing powder feeding rate. As a result, more energy is absorbed by the powder and the input energy to the substrate decreases, which reduces the depth of penetration. On the other hand, with increasing powder feeding rate, the height increases. The rise and fall in the height and depth of penetration can change the dilution.

The value of the wetting angle (θ), as the last geometric characteristic, was measured for all single-track deposits. The value changed from 11° to 83° . As shown in Fig. 13, the wetting angle depends on all three key process parameters. In

Fig. 11 The dilution as a function of key process parameters

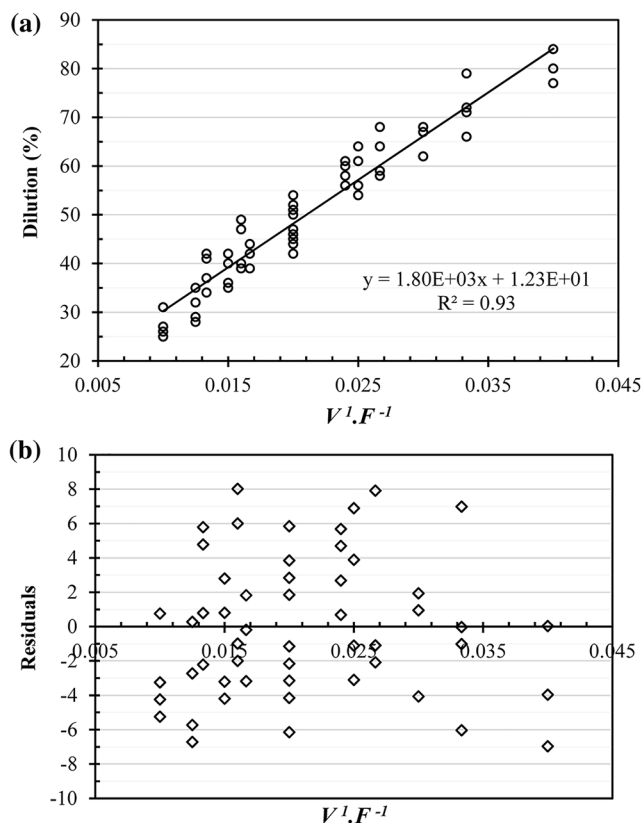
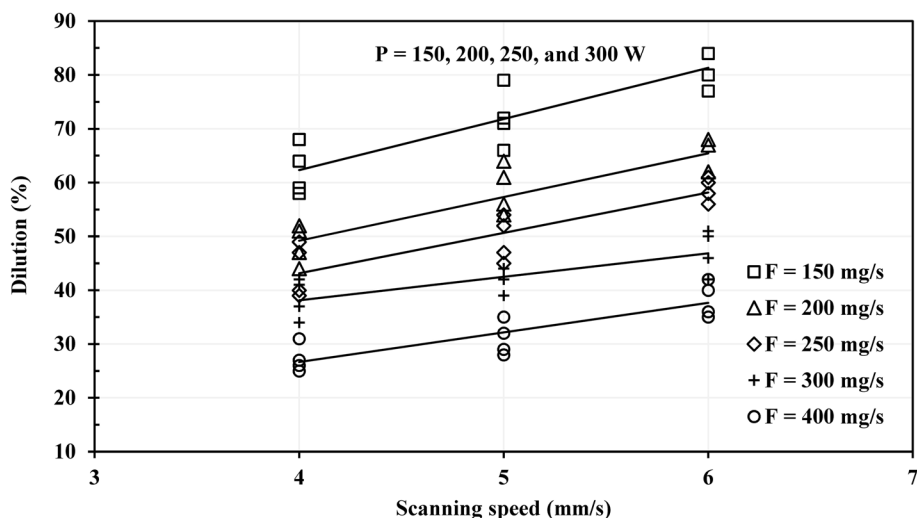


Fig. 12 **a** Dependency of the dilution on the combined parameter $V^1.F^{-1}$, and **b** residual plot

Fig. 14a, the relation between θ and the combined parameter $P^2V^{-1}F^1$ is depicted. Also, Fig. 14b shows the distribution of the residuals relative to the normal line. Assuming that the single-track deposits form a hemisphere, the wetting angle can be calculated by Eq. (3) [30].

$$\theta = 2 \arctan (2h/w) \tag{3}$$

By placing the values of h and w in Eq. (3), the values of calculated values of θ are very close to the values of θ measured experimentally. The analysis of the results indicated that θ has a direct relationship to the combined parameter of $P^2V^{-1}F^1$. The line equation for θ is specified as follows.

$$\theta = 9.26E - 06(P^2V^{-1}F^1) + 4.43E + 00$$

The combined parameter for the wetting angle in this paper is consistent with some previous research studies that reported a combined parameter including all three key process parameters [13, 19, 20, 23].

All predicted combined parameters with best correlations with measured geometric characteristics of single-track deposits are summarized in Table 4. All combined parameters with relatively high values of the linear regression coefficient ($R > 0.9$) were found showing the accuracy of all the directly measured quantities.

Based on the combined parameters, a process map was drawn. The drawing of this map helps to determine the best geometric characteristics. In general, using this map, the process parameters (P , V , and F) can be predicted according to desirable geometric characteristics. This can be done in reverse to predict geometric characteristics. On the other hand, according to the specification of the single-track deposits, it is possible to some extent predict the geometric characteristics of multi-track and/or single-wall deposits. The process map is plotted in Fig. 15. In this figure, the variations of laser power on the vertical axis and F/V on the first horizontal axis are indicated. The square points in the plot represent all combinations of process parameters used in this study. The lines and curves on this map represent all the modeling geometric features. The second horizontal axis highlights the dilution values. As the dilution does not depend on laser power (depends on the F/V ratio), it is possible to determine the dilution value for any given F/V ratio on the first horizontal axis. The advisable dilution percentages are drawn in the form of two fixed values

Fig. 13 The wetting angle as a function of key process parameters

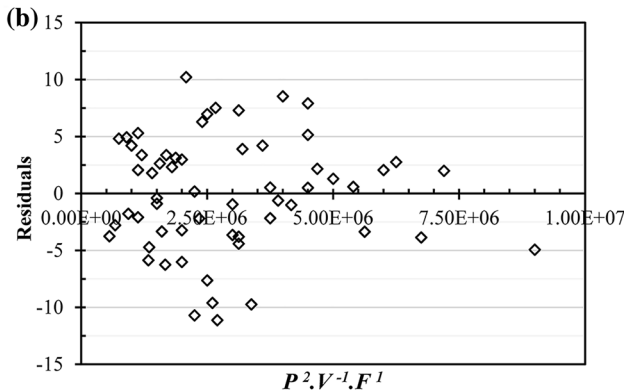
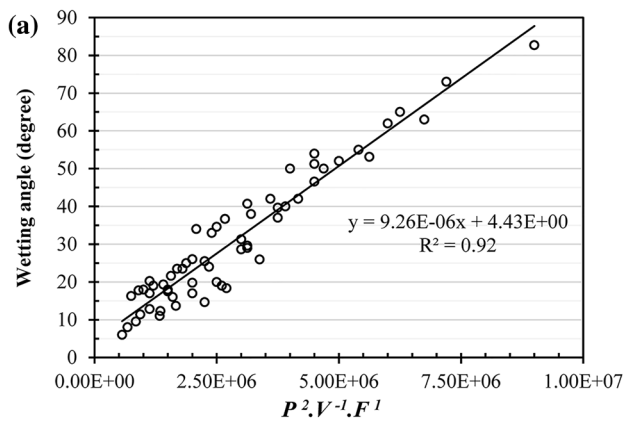
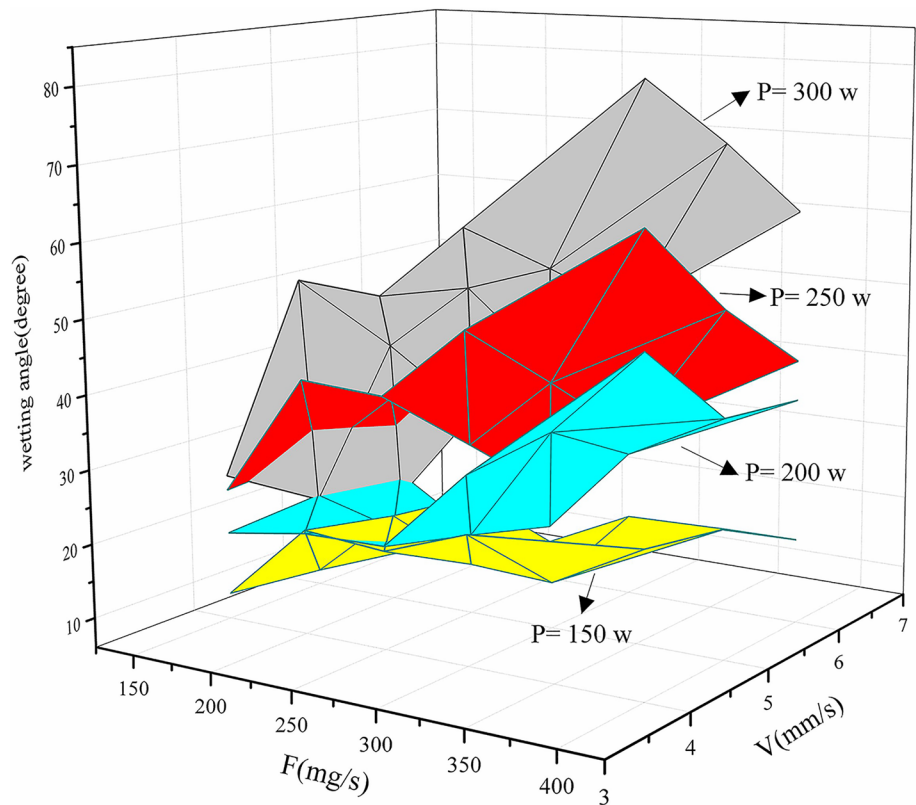


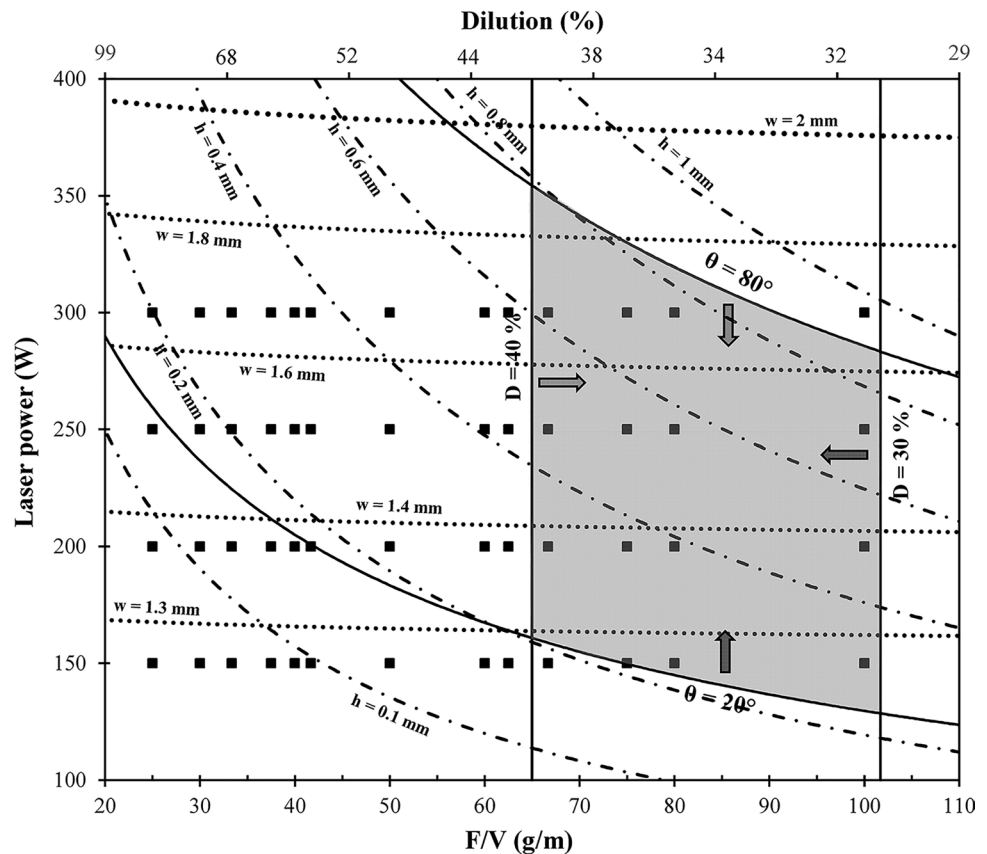
Fig. 14 **a** Dependency of the wetting angle on the combined parameter $P^2.V^{-1}.F^1$, and **b** residual plot

Table 4 All combined parameters obtained by linear regression method with the best correlations with measured geometric characteristics

Quantity (y)	Combined parameter (x)	R	a	b
h (mm)	$P^{3/2}V^{-1}F^1$	0.96	$1.94E-06$	$-5.30E-02$
w (mm)	$P^2V^{-1/4}$	0.97	$8.77E-06$	$1.14E+00$
b (mm)	$P^2.F^{-1}$	0.96	$7.36E-04$	$1.10E-01$
θ ($^\circ$)	$P^2V^{-1}F^1$	0.96	$9.26E-06$	$4.43E+00$
D (%)	V^1F^{-1}	0.96	$1.80E+03$	$1.23E+01$

of 30 and 40 percent as two solid vertical lines in Fig. 15. In this plot, the parabolic-dotted curves show the values of w for five fixed values of 1.3, 1.4, 1.6, 1.8 and 2 mm. Similar to w , the parabolic-dashed curves show the values of h for six fixed values of 0.1, 0.2, 0.4, 0.6, 0.8 and 1 mm. In Fig. 15, two fixed values of θ (20° and 80°) are plotted as two solid parabolic curves. A shaded region is indicated in this figure. If the process parameters were selected so that the combination of P and F/V located in this shaded region, the single-track deposits will have suitable geometric characteristics for multi-track and/or single-wall LADMD. Determination of optimal region (shaded) was conducted based on the results of previous research studies and the results obtained in this study. In the case of wetting angle, selecting the correct wetting angle prevents the formation of internal porosity. Therefore, the wetting

Fig. 15 Process map for LDMD of Inconel 718 superalloy



angle θ should be less than 80° . On the other hand, low θ causes heterogeneity of deposits (low height and high width). Therefore, θ is to be at least 20° .

The dilution between 30 and 40% for single-track deposits is acceptable because a portion of the energy in the multi-track process is absorbed by the previous adjacent track and the amount of dilution is reduced. Therefore, the optimal region was introduced between the dilution values of 30%–40% to ensure the proper metallurgical bond between the deposits. Using the process parameters within the optimal region, some single-wall deposits were produced. Figure 16 shows the cross-sectional view of single-wall deposits. It can be seen that these single walls were formed with minimum relevant defects, such as cracks, bonding errors in the interface, or porosities. This shows that the optimal process parameters are suitable for LDMD of Inconel 718.

4 Conclusion

Laser-aided direct metal deposition (LDMD) of Inconel 718 superalloy was performed and an empirical-statistical modeling was successfully developed using linear regression method. The relationship between the key process parameters and geometric characteristics of single-track

deposits were determined and the following conclusions can be drawn.

- The height was dependent on laser power, scanning speed, and powder feeding rate; however, the impact of laser power was more pronounced than that of scanning speed, and powder feeding rate. This relationship can be written as $P^{3/2}V^{-1}F^1$.
- The width was precisely controlled by a combined parameter including laser power and scanning speed. Powder feeding rate had no effect and it is possible to ignore its effect. The combined parameter was obtained in the form of $P^2V^{-1/4}$.
- The depth of penetration was proportional to the combined parameter as P^2F^{-1} . However, the dilution was proportional to V^1F^{-1} , which is independent of laser power.
- The wetting angle was controlled by the combined parameter as $P^2V^{-1}F^1$. In addition, the calculated values of the wetting angle using the width and height showed the correctness and accuracy of the measurements.
- A process map was designed based on experimental relationships that could predict geometric characteristics and determine the appropriate parameters for LDMD of Inconel 718 superalloy.

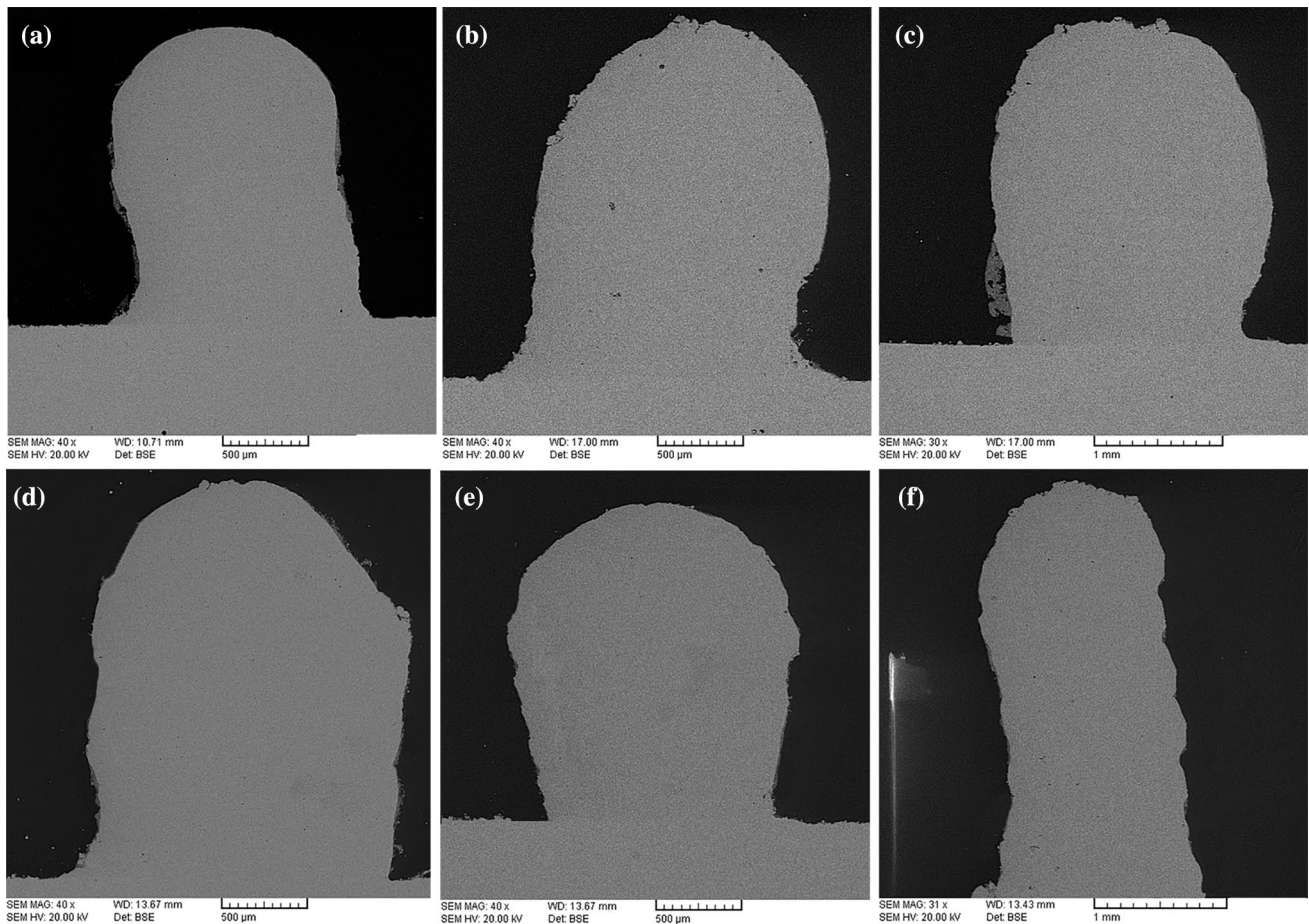


Fig. 16 SEM images of cross section of single-wall deposits with different process parameters; **a** P (250 W), V (4 mm/s), F (300 mg/s), Z-increment (0.4 mm); **b** P (250 W), V (4 mm/s), F (300 mg/s), Z-increment (0.3 mm); **c** P (300 W), V (5 mm/s), F (400 mg/s),

Z-increment (0.3 mm); **d** P (150 W), V (4 mm/s), F (400 mg/s), Z-increment (0.4 mm); **e** P (200 W), V (4 mm/s), F (400 mg/s), Z-increment (0.4 mm); **f** P (250 W), V (4 mm/s), F (400 mg/s), Z-increment (0.4 mm)

References

1. M. Dehmas, J. Lacaze, A. Niang, B. Viguier, TEM study of high-temperature precipitation of delta phase in Inconel 718 Alloy. *Adv. Mater. Sci. Eng.* **2011**, 1–9 (2011). <https://doi.org/10.1155/2011/940634>
2. S. Ghosh, S. Yadav, G. Das, Study of standard heat treatment on mechanical properties of Inconel 718 using ball indentation technique. *Mater. Lett.* **62**, 2619–2622 (2008). <https://doi.org/10.1016/j.matlet.2008.01.001>
3. A. Chamanfar, L. Sarrat, M. Jahazi, M. Asadi, A. Weck, A.K. Koul, Microstructural characteristics of forged and heat treated Inconel-718 disks. *Mater. Des.* **52**, 791–800 (2013). <https://doi.org/10.1016/j.matdes.2013.06.004>
4. C.-M. Kuoa, Y.-T. Yanga, H.-Y. Borb, C.-N. Weib, C.-C. Taia, Aging effects on the microstructure and creep behavior of Inconel 718 superalloy. *Mater. Sci. Eng. A* **510–511**, 289–294 (2009). <https://doi.org/10.1016/j.msea.2008.04.097>
5. S. Singh, S. Ramakrishna, R. Singh, Material issues in additive manufacturing: a review. *J. Manuf. Process.* **25**, 185–200 (2017). <https://doi.org/10.1016/J.JMAPRO.2016.11.006>
6. L. Li, A. Haghighi, Y. Yang, A novel 6-axis hybrid additive-subtractive manufacturing process: design and case studies. *J. Manuf. Process.* **33**, 150–160 (2018). <https://doi.org/10.1016/j.jmapro.2018.05.008>
7. M. Ansari, R. Shoja-Razavi, M. Barekat, H.C. Man, High-temperature oxidation behavior of laser-aided additively manufactured NiCrAlY coating. *Corros. Sci.* **118**, 168–177 (2017). <https://doi.org/10.1016/j.corsci.2017.02.001>
8. R. Conteri, T. Borkar, S. Nag, D. Jaeger, X. Chen, R.V. Ramanujan et al., Laser additive processing of Fe–Si–B–Cu–Nb magnetic alloys. *J. Manuf. Process.* **29**, 175–181 (2017). <https://doi.org/10.1016/J.JMAPRO.2017.07.029>
9. A. Ciraud, *Process and Device for the Manufacture of any Objects Desired from any Meltable Material* (FRG Disclosure Publication, Berlin, 1972), p. 2263777
10. L. Costa, I. Felde, T. Réti, Z. Kálazi, R. Colaço, R. Vilar et al., A simplified semi-empirical method to select the processing parameters for laser clad coatings. *Mater. Sci. Forum* **414–415**, 385–394 (2003). <https://doi.org/10.4028/www.scientific.net/MSF.414-415.385>
11. U. de Oliveira, V. Ocelík, J.T.M. De Hosson, Analysis of coaxial laser cladding processing conditions. *Surf. Coat. Technol.* **197**, 127–136 (2005). <https://doi.org/10.1016/j.surfcoat.2004.06.029>
12. J. Paulo Davim, C. Oliveira, A. Cardoso, Laser cladding: an experimental study of geometric form and hardness of coating using

- statistical analysis. *Proc. Inst. Mech. Eng. Part B J. Eng. Manuf.* **220**, 1549–1554 (2006)
13. V. Ocelik, U. de Oliveira, M. de Boer, J.T.M. de Hosson, Thick Co-based coating on cast iron by side laser cladding: analysis of processing conditions and coating properties. *Surf. Coat. Technol.* **201**, 5875–5883 (2007). <https://doi.org/10.1016/j.surfcoat.2006.10.044>
 14. J. Paulo Davim, C. Oliveira, A. Cardoso, Predicting the geometric form of clad in laser cladding by powder using multiple regression analysis (MRA). *Mater. Des.* **29**, 554–557 (2008). <https://doi.org/10.1016/j.matdes.2007.01.023>
 15. Y. Sun, M. Hao, Statistical analysis and optimization of process parameters in Ti6Al4 V laser cladding using Nd:YAG laser. *Opt. Lasers Eng.* **50**, 985–995 (2012). <https://doi.org/10.1016/j.optlaseng.2012.01.018>
 16. H. El Cheikh, B. Courant, S. Branchu, J.-Y. Hascoët, R. Guillén, Analysis and prediction of single laser tracks geometrical characteristics in coaxial laser cladding process. *Opt. Lasers Eng.* **50**, 413–422 (2012). <https://doi.org/10.1016/j.optlaseng.2011.10.014>
 17. S. Kumar, V. Sharma, A.K.S. Choudhary, S. Chattopadhyaya, S. Hloch, Determination of layer thickness in direct metal deposition using dimensional analysis. *Int. J. Adv. Manuf. Technol.* **67**, 2681–2687 (2013). <https://doi.org/10.1007/s00170-012-4683-1>
 18. S. Saqiba, R.J. Urbanica, K. Aggarwal, Analysis of laser cladding bead morphology for developing additive manufacturing travel paths. *Procedia CIRP* **17**, 824–829 (2014). <https://doi.org/10.1016/j.procir.2014.01.098>
 19. M. Barekat, R. Shoja Razavi, A. Ghasemi, Nd:YAG laser cladding of Co–Cr–Mo alloy on γ -TiAl substrate. *Opt. Laser Technol.* **80**, 145–152 (2016). <https://doi.org/10.1016/j.optlastec.2016.01.003>
 20. M. Ansari, R. Shoja Razavi, M. Barekat, An empirical-statistical model for coaxial laser cladding of NiCrAlY powder on Inconel 738 superalloy. *Opt. Laser Technol.* **86**, 136–144 (2016). <https://doi.org/10.1016/j.optlastec.2016.06.014>
 21. X. Shi, S. Ma, C. Liu, Q. Wu, Parameter optimization for Ti–47Al–2Cr–2Nb in selective laser melting based on geometric characteristics of single scan tracks. *Opt. Laser Technol.* **90**, 71–79 (2017). <https://doi.org/10.1016/j.optlastec.2016.11.002>
 22. M. Erfanmanesh, H. Abdollah-Pour, H. Mohammadian-Semnani, R. Shoja-Razavi, An empirical-statistical model for laser cladding of WC-12Co powder on AISI 321 stainless steel. *Opt. Laser Technol.* **97**, 180–186 (2017). <https://doi.org/10.1016/j.optlastec.2017.06.026>
 23. M. Nabhani, R. Shoja Razavi, M. Barekat, An empirical-statistical model for laser cladding of Ti–6Al–4V powder on Ti–6Al–4V substrate. *Opt. Laser Technol.* **100**, 265–271 (2018). <https://doi.org/10.1016/j.optlastec.2017.10.015>
 24. M. Erfanmanesh, R. Shoja-Razavi, H. Abdollah-Pour, H. Mohammadian-Semnani, Influence of using electroless Ni–P coated WC–Co powder on laser cladding of stainless steel. *Surf. Coat. Technol.* (2018). <https://doi.org/10.1016/j.surfcoat.2018.05.016>
 25. E. Toyserkani, A. Khajepour, S. Corbin, *Laser Cladding* (CRC Press, Boca Raton, 2004)
 26. Y. Fu, A. Loreda, B. Martin, A.B. Vannes, A theoretical model for laser and powder particles interaction during laser cladding. *J. Mater. Process. Technol.* **128**, 106–112 (2002). [https://doi.org/10.1016/S0924-0136\(02\)00433-8](https://doi.org/10.1016/S0924-0136(02)00433-8)
 27. I. Tabernero, A. Lamikiz, S. Martínez, E. Ukar, L.N. López De Lacalle, Modelling of energy attenuation due to powder flow-laser beam interaction during laser cladding process. *J. Mater. Process. Technol.* **212**, 516–522 (2012). <https://doi.org/10.1016/j.jmatprotec.2011.10.019>
 28. W. Devesse, D. De Baere, P. Guillaume, Modeling of laser beam and powder flow interaction in laser cladding using ray-tracing. *J. Laser Appl.* **27**, S29208 (2015). <https://doi.org/10.2351/1.4906394>
 29. W.M. Steen, J. Mazumder, *Laser Material Processing*, 4th edn. (Springer, London, 2010). <https://doi.org/10.1007/978-1-84996-062-5>
 30. H.-J. Bartsch, *Geometry. Handbook of Mathematical Formulas* (Academic Press, New York, 1974), p. 155. <https://doi.org/10.1016/b978-0-12-080050-6.50007-5>

Publisher's Note Springer Nature remains neutral with regard to jurisdictional claims in published maps and institutional affiliations.